Hydrodynamic dispersion in thin channels with micro-structured porous walls

Bowen Ling, Mart Oostrom, Alexandre M. Tartakovsky, and Ilenia Battiato

Citation: Physics of Fluids **30**, 076601 (2018); doi: 10.1063/1.5031776
View online: https://doi.org/10.1063/1.5031776
View Table of Contents: http://aip.scitation.org/toc/phf/30/7
Published by the American Institute of Physics

Hydrodynamic dispersion in thin channels with micro-structured porous walls

Bowen Ling,[1] Mart Oostrom,[2,a)] Alexandre M. Tartakovsky,[3] and Ilenia Battiato[1,b)]
[1]*Department of Energy Resources Engineering, Stanford University, Stanford, California 94305, USA*
[2]*Environmental Molecular Science Laboratory, Pacific Northwest National Laboratory, Richland, Washington 99354, USA*
[3]*Fundamental and Computational Science Directorate, Pacific Northwest National Laboratory, Richland, Washington 99354, USA*

(Received 30 March 2018; accepted 18 June 2018; published online 12 July 2018)

Flow and transport within porous- and microtextured-walled channels is relevant to a number of natural and industrial processes. Designing and optimizing the topology of the pores and/or microstructure to achieve target performance at the system scale (or macroscale) is still an open question. In this work, we study whether hydrodynamic dispersion in microfluidic channels with walls structured by obstacles can be modeled by dispersion in channels with porous walls described as continuous porous media of zero or finite permeability. We perform single phase microfluidic non-reactive flow experiments in channels embedded in micropatterns with different topologies. Specifically, we focus on transverse riblets and arrays of pillars as examples of impermeable and permeable obstructions, respectively. We compare the experimental results with three models: 3D pore-scale simulations which resolve the micropattern geometry explicitly and two upscaled models which treat the micropattern as a continuum of zero or finite permeability. This study demonstrates that polydimethylsiloxane micromodels with appropriately patterned surfaces can be successfully employed to validate various continuum-scale modeling approximations in different physical regimes, identified by the order of magnitude of the Péclet number and the obstruction permeability. *Published by AIP Publishing.*
https://doi.org/10.1063/1.5031776

I. INTRODUCTION

A variety of natural and industrial processes are characterized by flow and transport within porous- or (micro)textured-walled channels. Some examples include contaminant transport in fractured rocks, flows over sediment beds (Goharzadeh *et al.*, 2005; Nikora *et al.*, 2001; and Liu *et al.*, 2013), vegetation (Papke and Battiato, 2013; Battiato and Rubol, 2014; Rubol *et al.*, 2016; and Rubol *et al.*, 2018) and slippery liquid-infused porous surfaces (Cui *et al.*, 2015 and Hou *et al.*, 2015), and ultrafiltration of colloids (Maruf *et al.*, 2013), just to mention a few. Examples of flows over micropatterns in the form of, e.g., villi, posts, riblets, etc., include nutrient uptake from roots (Marschner and Dell, 1994 and Gilroy and Jones, 2000), flows above carbon nanotube (CNT) forests and superhydrophobic surfaces (Deck *et al.*, 2009; Battiato, 2012; and 2014), nutrient delivery in micro-fluidic bioreactor devices (Gruenberger *et al.*, 2013 and Griffiths *et al.*, 2013), and chaotic mixing in microchannels (Stroock and Whitesides, 2003 and Stroock *et al.*, 2002).

While seemingly different, these systems share some unique features: their overall macroscopic response is regulated by the exchange of mass and momentum through the shared channel-obstruction interface and by the obstruction topology. Yet, relating the (pore-scale) obstruction topology to the response function at the system scale remains largely unaddressed (Bouquet and Lauga, 2011).

Direct numerical simulations, which explicitly resolve the obstruction topology, are often too computationally intensive when a great disparity of scales between the micropattern and the device (or system) exists. When direct numerical simulations do not represent a viable option due to their computational cost, two complementary approaches can be employed. On the one hand, microfluidic devices have been a well-vetted experimental tool to study transport in porous media and through arrays of obstacles (riblets, pillars, etc.). However, their unit cost may be relatively high and this may significantly hinder one's practical ability to fully explore the topology parameter space.

An alternative approach is to use upscaled (effective, macroscopic) models, where the obstruction is treated as a porous continuum/matrix (and not as an array of discrete obstacles) (Griffiths *et al.*, 2013; Dejam *et al.*, 2014; and Ling *et al.*, 2016). Yet, existing effective models that describe flow and transport in channel-matrix systems have rarely been experimentally tested nor validated in the context of microfluidic devices: this is because the use of microtextured channels to validate upscaled models presents its unique challenges (as opposed to microchannels whose entire cross section is occupied by obstacles).

The main question is whether a few layers of discrete obstacles can be modeled as an effective continuum, and

[a)]Present address: INTERA Incorporated, 3240 Richardson Road, Suite 2, Richland, WA 99354.
[b)]Electronic mail: ibattiat@stanford.edu.

consequently, whether or not microfluidics experiments in microchannels with textured/patterned walls could be both employed as surrogates of more complex channel-matrix coupled systems and used to validate existing theories. In fact, besides dynamic constraints (Battiato and Tartakovsky, 2011; Ling *et al.*, 2016; and Korneev and Battiato, 2016), the underlying assumption of any upscaled model is that separation of geometrical length scales between the micro- and macro-scale exists (Wood, 2009); i.e., the typical length scale associated with the obstacles (e.g., their mean diameter d) should be much smaller than a characteristic length at the macroscale (e.g., the length of the microfluidic chip L). This constraint guarantees the existence of a Representative Elementary Volume (or REV) of size W such that $d \ll W < L$, where W is the entire width of the obstruction/patterned region. This condition can be easily enforced by design when the microchip is occupied by solid obstacles throughout its width (Willingham *et al.*, 2010 and Zhang *et al.*, 2010). However, when the obstacles do not occupy the entire cross section of the microchannel, due to the presence of a preferential flow path (i.e., fracture/channel), the identification of an appropriate REV may be problematic and micromodels' capability to serve as appropriate surrogate systems for the validation of theoretical models of channel-matrix dynamics becomes uncertain. Although a number of studies have successfully employed porous media theory to describe mean flow and transport through a variety of micro-patterned channels and pipes ranging from viscous flow over microvilli in capillaries, microscopic cellular membrane protrusions with hair-like structures (e.g., Weinbaum *et al.*, 2003), to turbulent flows over CNT forests and vegetation (e.g., Battiato *et al.*, 2010 and Battiato, 2014), no experimental study exists to support the validity of such an approximation, whose schematic is shown in Fig. 1.

Here, we focus on passive solute transport in thin porous channels with controlled microtexture and study whether hydrodynamic dispersion in microfluidic channels with walls structured by obstacles can be modeled by dispersion in channels with porous walls described as continuous porous media of zero or finite permeability. In this work, we combine local optical measurements, upscaled models, and fully resolved pore-scale 3D computational dynamics simulations to investigate the validity of such an assumption. Specifically, we compare experimental data from microfluidic cells patterned with different topologies (transverse riblets and arrays of cylinders) with fully resolved pore-scale simulations and two macroscopic transport models developed by Dejam *et al.* (2014) and Ling *et al.* (2016) that account for either purely diffusive or dispersive transport in the matrix, respectively. The scope of the study is twofold. On the one hand, we demonstrate that patterned microfluidic chips can be used as experimental surrogates of channel-matrix systems, and on the other hand, we examine the influence of pore-scale matrix topology on macroscale (continuum-scale) solute dispersion. Importantly, these sets of experiments can be used to directly assess whether or not a continuum approximation is valid in the presence of a limited number of obstacles (Valdes-Parada *et al.*, 2009). Furthermore, the experiments are designed to highlight the significance and influence of the obstruction geometry (particularly as it affects its permeability) on the accuracy of the two upscaled models in different Péclet number regimes and to develop a phase diagram to identify the applicability conditions of each macroscopic solution.

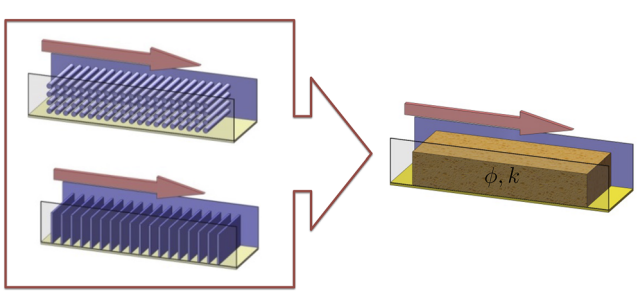

FIG. 1. Conceptualization of the possible linkage between (microfluidic) experiments in channels with controlled microtexture (left) and models of coupled channel-matrix systems (right) where any array of discrete obstacles composing the matrix is treated as a porous continuum with effective properties, e.g., porosity ϕ and permeability k.

The paper is organized as follows: Sec. II describes the experimental setup, the calibration procedure, and the experimental matrix. In Sec. III, we present the setup of our three-dimensional simulations and review the analytical macroscopic models describing passive transport in a thin channel embedded in permeable (Ling *et al.*, 2016) and impermeable (Dejam *et al.*, 2014) matrices. Experimental and numerical results are discussed in Sec. IV. We conclude with Sec. V.

II. EXPERIMENTAL SETUP

A. Micromodel fabrication

The micromodels used in this study have been fabricated at the Pacific Northwest National Laboratory, applying standard microphotolithography techniques. First, the flow layer features, including the channel and the porous matrix, are printed on a mask, Fig. 2. A separate silicon wafer is then spin-coated with an SU-8 photoresist before the wafer is exposed to UV light with the printed mask placed on top of it. The exact same pattern is created on the silicon wafer during the developing process. The silicon wafer is subsequently placed on a hot plate for heat treatment at a temperature of 180 °C and kept for 30 min. After this treatment, the developed features have a depth $H_z = 80.0\ \mu$m, equal to the depth of the channel, see Fig. 3 for a view of the microchannel geometry, while the depth of the inlet structure is 28.0 μm in order to provide complete sealing from the control layer. The channel length is $L = 15$ mm, the fracture aperture is $2b = 0.5$ mm, and the pattern width is $W = 1.5$ mm (see Fig. 2). The cell depth is designed based on the typical Hele-Shaw cell length ratio (0.1–1) between the depth and the characteristic length scale of the pore geometry which, in our study, is the shortest distance between obstacles (i.e., pore throat) (Ul Islam and Gandhi, 2016). A mixture of polydimethylsiloxane (PDMS) base and PDMS curing agent is employed to produce replicas of the silicon micromodels using the wafer as the mold. PDMS is poured onto the wafer and, after the curing process, the flow layer of the micromodel is obtained, Fig. 2. A control layer is bound to the flow layer to keep the interior surfaces uniform and to control the inlet flow. The control layer is patterned with an air valve,

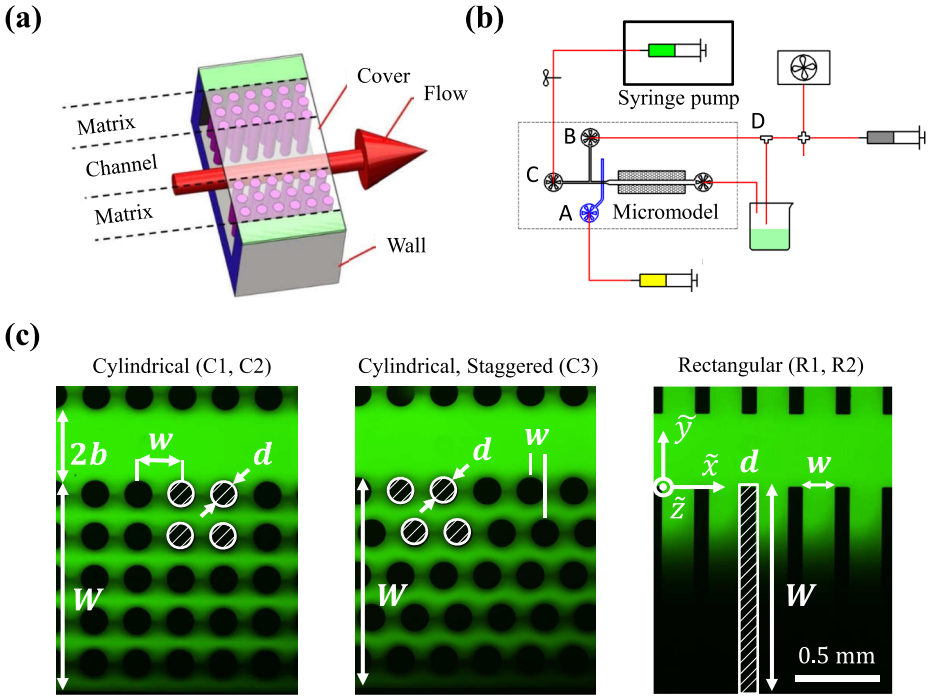

FIG. 2. Schematics of the experimental setup: (a) axonometric view of a portion of the micromodel where the microstructures occupy the entire depth of the micromodel; the flow direction is indicated by the red arrow; (b) exterior flow system; (c) top view of portions of three micromodels with different matrix topologies. Dye concentration increases with the green color intensity.

a thin elastomeric membrane which deforms when air pressure (~10 psi) is applied. The membrane, beneath the flow channel, bends toward the interior surface of the channel when air is injected beneath it. The deformed membrane seals the flow channel to prevent premixing in the external piping system, while ensuring that the concentration of the incoming solution is uniform. In the final fabrication step, the micromodel is bounded to a glass slide using plasma and cured for 12 h at 75 °C.

Alexa Flour 488 (ThermoFisher Scientific, Inc., San Diego, CA), a green fluorescent dye, is used for visualization and measurement of the concentration in the micromodels. The initial concentration (c_0) of the dye solution is 34.40 μmol l^{-1}. The molecular diffusion coefficient of Alexa 488 in water is $D_0 = 4.35 \times 10^{-10}$ m^2 s^{-1} at 20 °C (Petrášek and Schwille, 2008). Other properties (e.g., viscosity and density) of the dilute dye solution are considered the same as those of deionized (DI) water. In all experiments, the laboratory temperature is set to 21 ± 0.5 °C. Thus, all fluid and transport properties are assumed to be constant throughout all experiments. The micromodels are placed on a motorized stage (Prior Scientific Instrument, Inc., Rockland, MA), controlled by NIS-Elements (Nikon, Melville, NY) software, and images of fluorescent intensity fields are recorded by a CCD camera attached to a Nikon Ti Epi-fluorescence microscope (Nikon, Melville, NY) with a 4× objective. During each experiment, typically lasting approximately 30 min, 500-1500 pictures are taken. In every experiment, the micromodel is first saturated with DI-water, using inlet B before injection of the dye solution; see Fig. 2(b). After visual inspection of the saturation, water injection is interrupted. To prevent pre-mixing during this phase in the exterior tubing system, the air valve [A in Fig. 2(b)] is kept closed. The dye solution is then injected from inlet C [Fig. (2b)] by using a syringe pump (New Era, Farmingdale, NY) at a constant volumetric flow rate (Q). Since the dye solution would occupy the tubing components between valves A, B, and C, at the beginning of the dye injection experiment, valve A is opened, while B is closed. After each experiment, the tubing system and the micromodel are thoroughly cleaned.

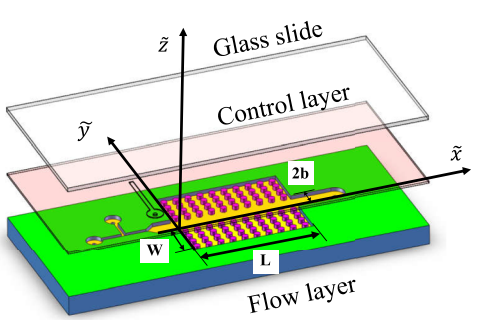

FIG. 3. Micromodel design with a valve system.

The concentration of the fluorescent solute is computed using intensity-concentration calibration curves, $c(I)$, where c [-] is the concentration normalized by the inlet concentration c_0 and I [-] is the light intensity. To prevent ambient light pollution during the measurement, the micromodel is covered by black foil. First, we test several exposure times to determine those that lead to the best linear relationship between light intensity, I, and concentration, c, as shown in Fig. 4. The calibration is performed using the linear relationship

$$I_1 = I_0 + \alpha c, \tag{1}$$

where α is the calibration constant and I_0 and I_1 are the light intensities measured in zero-concentration and fully fluorescence saturated domains (the inset of Fig. 4), respectively. The results show that an exposure time of 75 ms yields the best linearity (with $\alpha = 1.56 \times 10^4$ [-]). As a result, the exposure time was set to 75 ms in all experiments.

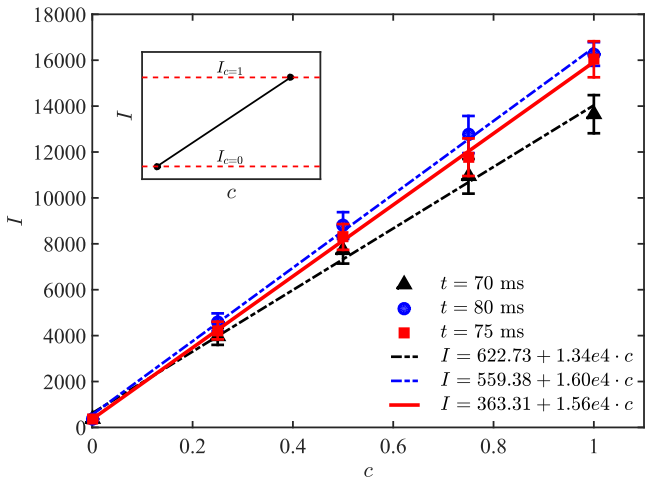

FIG. 4. Intensity-concentration relations for three exposure times. The error bar represents three standard deviations.

B. Obstruction topology and experimental matrix

To test the ability of patterned microchannels to act as surrogates of coupled channel/porous medium flow systems, we design different pattern geometries to represent both highly permeable and nearly impermeable matrices: (i) aligned and staggered cylindrical posts (referred to as C structures) and (ii) rectangular riblets perpendicular to the main flow direction (referred to as R structures), respectively. The experimental matrix is listed in Table I.

The different matrix structures and obstacles' dimensions are illustrated in Table I. The C structures have 5 rows of aligned or staggered cylinders. The transverse riblets can model matrices with zero longitudinal permeability since the net flux through the pattern is zero in the flow direction. While the matrix structures considered in this study may rather accurately represent typical topologies in engineered systems, they greatly deviate from natural porous media, e.g., rocks. However, spatially periodic representations of micro-structures of geologic porous media are routinely used to derive macroscopic properties and effective models of phenomena taking place in disordered, but statistically homogeneous, media that lack such periodicity [Whitaker (1999); Hornung (1997); and Nitsche and Brenner (1989), Sec. 2 and the references therein]. Experiments are performed at three different Péclet numbers, Pe, for each configuration with

$$\mathrm{Pe} := \frac{Ub}{D_0}, \tag{2}$$

where

$$U = \frac{Q}{2bH_z} \tag{3}$$

is the inlet mean velocity, b and H_z are the channel half-width and depth, respectively, and D_0 is the molecular diffusion coefficient. Concentration transect data at one location (i.e., the center of the channel, at $\tilde{x} = 8$ mm) along the flow direction are collected.

In Fig. 5, we plot the measured breakthrough curves (BTCs) for the entire experimental matrix. In Sec. III, we present the three models used to predict the experimental BTCs.

TABLE I. Overview of experimental conditions: volumetric flow rate Q, Péclet number Pe, structure porosity ϕ, and obstacles' dimensions d and w, as defined in Fig. 2. For all micromodels, the chip's length and depth are $L = 15$ mm and $H_z = 80.0$ μm, respectively, the porous matrix width is $W = 1.5$ mm, and the channel aperture is $b = 0.25$ mm.

		Q (μl h^{-1})	Péclet (-)	ϕ (-)	d (mm)	w (mm)
	C1-10	10	40.3			
	C1-50	50	201.9	0.65	0.08	0.12
	C1-100	100	403.7			
	C2-10	10	40.3			
	C2-50	50	201.9	0.48	0.24	0.3
	C2-100	100	403.7			
	C3-10	10	40.3			
	C3-50	50	201.9	0.65	0.08	0.04
	C3-100	100	403.7			
	R1-10	10	40.3			
	R1-50	50	201.9	0.65	0.11	0.2
	R1-100	100	403.7			
	R2-10	10	40.3			
	R2-50	50	201.9	0.48	0.11	0.1
	R2-100	100	403.7			

III. MODEL FORMULATION

In this study, we compare the experimental breakthrough curves measured at the center of the channel with those calculated from three different models, one at the pore-scale and two at the continuum-scale. The models are discussed in the following.

A. Pore-scale equations and numerical model validation

Incompressible flow and passive transport at the pore-scale is described by the incompressible Navier-Stokes equation and the advection-diffusion equation (ADE) in three dimensions,

$$\frac{\partial \tilde{\mathbf{u}}}{\partial \tilde{t}} + (\tilde{\mathbf{u}} \cdot \tilde{\nabla})\tilde{\mathbf{u}} + \frac{1}{\rho}\tilde{\nabla}\tilde{P} = \tilde{\nabla} \cdot (\nu \tilde{\nabla}\tilde{\mathbf{u}}), \quad \tilde{\nabla} \cdot \tilde{\mathbf{u}} = 0, \tag{4a}$$

$$\frac{\partial c}{\partial \tilde{t}} + \tilde{\mathbf{u}} \cdot \tilde{\nabla} c - D_0 \tilde{\nabla}^2 c = 0, \tag{4b}$$

where c [-] is the concentration normalized by the inlet concentration c_0, $\tilde{\mathbf{u}} = [\tilde{u}, \tilde{v}, \tilde{w}]$ is the dimensional velocity vector field, $\tilde{P}$ is the dimensional pressure, and ρ and ν are the density and kinematic viscosity of the fluid, respectively. Since we consider aqueous dilute solutions, the density and viscosity are set to those of water, $\rho = 1000$ kg/m^3 and $\nu = 10^{-6}$ m^2/s. The physical boundaries of the simulation domain are shown in Fig. 6(a), where we only model half of the entire chip (a symmetry boundary condition is imposed along the channel axis, Γ_c). The inlet and outlet boundaries are denoted as Γ_i and Γ_o, respectively, while Γ_w denotes all the impermeable walls, i.e., obstacles, top/bottom surfaces, and any other solid surface

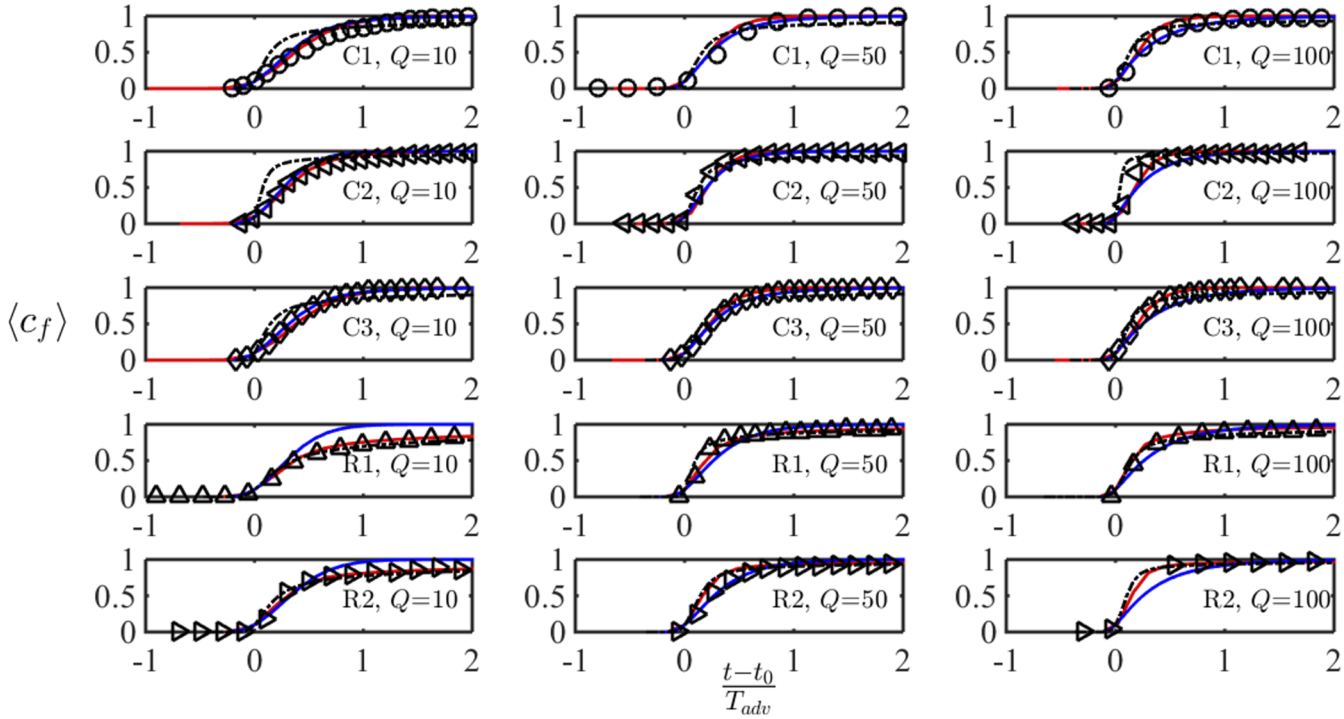

FIG. 5. Comparison of breakthrough curves from the experiments (hollow black markers), 3D simulations (solid red lines), diffusive model (black dashed lines), and dispersive model (solid blue lines). The physical time is rescaled and normalized: t_0 represents the time when $c = 0.1$ and $T_{adv} = L/U$.

of the chip. The constant inlet flow rate is imposed on Γ_i to exactly match the experimental conditions, i.e.,

$$\tilde{\mathbf{u}} = (U, 0, 0), \quad \mathbf{n} \cdot \tilde{\nabla}\tilde{P} = 0 \quad \text{for} \quad \tilde{\mathbf{x}} \in \Gamma_{\mathrm{i}}, \tag{5a}$$

$$\mathbf{n} \cdot \tilde{\nabla}\tilde{\mathbf{u}} = 0, \quad \tilde{P} = \tilde{P}_{\mathrm{out}} \quad \text{for} \quad \tilde{\mathbf{x}} \in \Gamma_{\mathrm{o}}, \tag{5b}$$

$$\tilde{\mathbf{u}} = \mathbf{0}, \quad \mathbf{n} \cdot \tilde{\nabla}\tilde{P} = 0 \quad \text{for} \quad \tilde{\mathbf{x}} \in \Gamma_{\mathrm{W}}, \tag{5c}$$

$$\mathbf{n} \cdot \tilde{\nabla}\tilde{\mathbf{u}} = 0, \quad \mathbf{n} \cdot \tilde{\nabla}\tilde{P} = 0 \quad \text{for} \quad \tilde{\mathbf{x}} \in \Gamma_{\mathrm{c}}, \tag{5d}$$

where $\tilde{\mathbf{x}}$ is the position vector, $\tilde{P}_{\mathrm{out}}$ is set to ambient pressure (i.e., $\tilde{P}_{\mathrm{out}} = 0$), U is the inlet mean velocity defined by (3), and the experimental volumetric flow rates Q are listed in Table I. For transport, we impose a continuous injection (Dirichlet) condition at the inlet $c = 1$ and a zero-gradient boundary condition at the outlet, together with symmetry conditions on Γ_c. The three-dimensional geometry of the chip is imported directly from the design drawings of the experimental chips. The only difference between the real chip and the reconstructed one is in the length of the inlet rectangular channel, which is reduced to curb computational costs of the 3D simulations. The system of Eqs. (4) and (5) is solved using OpenFoam®. Meshing and pre-processing are performed using the OpenFoam mesh generator, SnappyHexMesh. An example of the mesh detail is shown in Fig. 6(b). We use 12 mesh cells in the z-direction. The minimum number of cells in the thinnest pore throats is 12. The 3D models for cells with C1, C2,

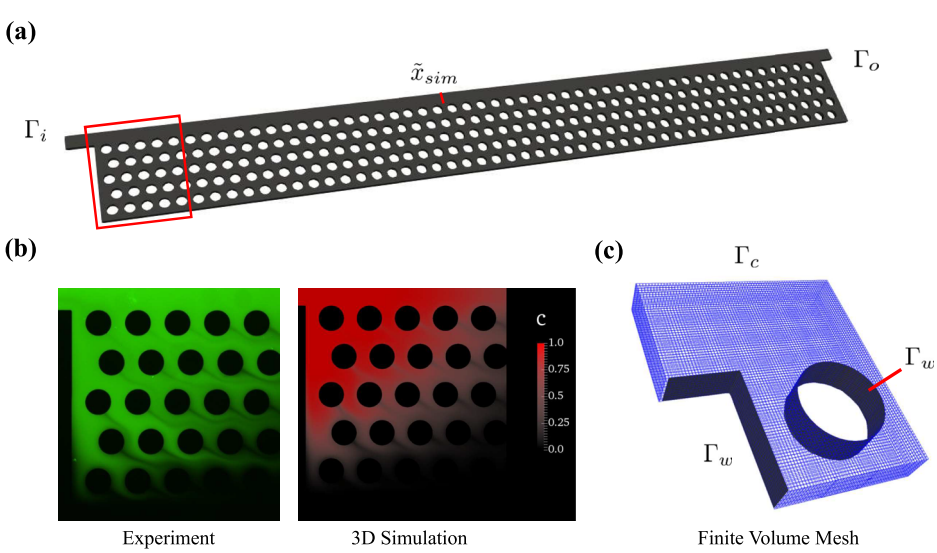

FIG. 6. (a) Three-dimensional computational domain for matrix topology C3; (b) concentration field from the experiments (left) and simulation (right) under the same condition; (c) finite volume mesh near the inlet.

C3, R1, and R2 pore geometries have between 6 000 000 and 7 000 000 elements. Figure 6(c) shows good agreement between the pore-scale concentration distribution imaged in one of the experiments and the corresponding simulated concentration field at the same location. Direct numerical simulations are used both to make direct predictions of the experimental breakthrough curves and to parametrize upscaled models (as discussed in Sec. III B). We emphasize that the 3D simulations have no fitting parameters. The difference in the concentration arrival time (e.g., the time t_0 when $c = 0.1$) between the experiments and simulations due to a difference in the simulated entrance length is addressed by accounting for the time shift t_0, i.e., the physical time $\tilde{t}$ is rescaled as

$$t = \frac{\tilde{t} - t_0}{T_{adv}}, \tag{6}$$

where T_{adv} is the advective time scale $T_{adv} = L/U$. The BTCs predicted by direct numerical simulations are overlaid to the experimental ones in Fig. 5 (red lines). Among most simulations (14 out of 15), the 3D model predictions have an average percentage error of $E^{\%} = 6\%$ or less, as shown in Fig. 7, with

$$E^{\%} = \frac{1}{N}\sum_{i=1}^{N}\frac{|\langle c_f\rangle_{i,3D} - \langle c_f\rangle_{i,Data}|}{\langle c_f\rangle_{i,Data}}, \tag{7}$$

where N is the number of experimental data points for each run. Once the code has been validated, the 3D pore-scale simulations can be used (i) as a virtual laboratory to directly study the impact of micropattern topology on macroscale dispersion and (ii) to investigate the validity of some of the approximations of macroscopic models, where the pattern is treated as an effective porous medium, as described in Sec. III B.

B. Upscaled models

From a theoretical point of view, the difficulty of studying solute transport in micropatterned channels lies (i) in the dynamic coupling between the two regions (channel of aperture $2b$ and obstruction/matrix of width W, Fig. 2) and (ii) in the need to incorporate different geometrical properties of the matrix into flow and solute transport models at larger scales (macroscale). Under the hypothesis that an array of discrete obstacles can be treated as a porous continuum, both objectives are addressed by mathematical upscaling (e.g., homogenization method, stochastic homogenization, and volume averaging). These techniques are employed to derive 1D macroscopic models for the average concentration in the channel $\langle c_f\rangle(x,t)$ [and the matrix $\langle c_m\rangle(x,t)$] under the assumption of a thin channel (i.e., $b \ll L$) and to determine the effective dispersion coefficient in the channel in terms of matrix properties. Yet, most one-dimensional thin channel models (Tang *et al.*, 1981 and Dejam *et al.*, 2014), as well as two-dimensional dispersion models (Roubinet *et al.*, 2012), assume purely diffusive transport in the matrix and routinely neglect its permeability or any dispersive transport in it. Only recently, attempts to account for matrix permeability have been undertaken (Griffiths *et al.*, 2013 and Ling *et al.*, 2016). For example, Ling *et al.* (2016) utilize perturbation theory and upscaling techniques to obtain the channel dispersion coefficient in terms of matrix porosity and permeability. Notwithstanding the existence of numerous theoretical models to characterize mean concentration distribution in such coupled systems, there is no experimental evidence of their validity or regimes of applicability. Additionally, most macroscale models contain parameters that cannot be determined from experiments either because they are primarily empirical factors that cannot be clearly related to a specific physical process or because they may be difficult to measure. As a result, identification of a relationship between the pore-scale matrix structure and channel dispersion becomes challenging.

In this section, we compare the experimental concentration data with two upscaled models of passive transport in coupled channel-matrix systems for non-permeable (Dejam *et al.*, 2014) and permeable (Ling *et al.*, 2016) matrices and investigate the impact of pore geometry on the macroscopic concentration field. Both solutions describe the spatio-temporal evolution of the dimensionless concentration in the channel and the matrix averaged over the channel and matrix width, $\langle c_f\rangle$ and $\langle c_m\rangle$, where $\langle\cdot\rangle$ defines an averaging operator

$$\langle\cdot\rangle = \frac{1}{L^\star}\int_0^{L^\star}\cdot\,\mathrm{d}y, \tag{8}$$

where $L^\star = 1$ is the dimensionless channel width and $L^\star = -h$ with $h = W/b$ being the dimensionless matrix width. In the following, we refer to the two models proposed by Dejam *et al.* (2014) and Ling *et al.* (2016) as "diffusive-matrix" and "dispersive-matrix" models, respectively.

1. Diffusive-matrix model

Under the hypothesis that the discrete obstacles can be treated as a porous continuum impermeable to flow, where mass transport is entirely controlled by diffusion from the channel into the matrix, the average concentration in the channel and the concentration in the matrix, $\langle c_f\rangle$ and c_m, satisfy

$$\epsilon\mathrm{Pe}\frac{\partial\langle c_f\rangle}{\partial t} + \epsilon\mathrm{Pe}\frac{7}{5}V_m\frac{\partial\langle c_f\rangle}{\partial x} = \epsilon^2 D_d\frac{\partial^2\langle c_f\rangle}{\partial x^2} - 3(\langle c_f\rangle - \langle c_m\rangle), \tag{9a}$$

$$\epsilon\mathrm{Pe}\frac{\partial c_m}{\partial t} = D_m\frac{\partial^2 c_m}{\partial y^2}, \tag{9b}$$

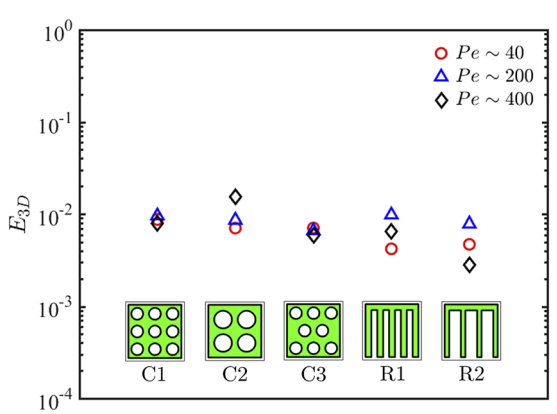

FIG. 7. Average percentage error, defined in (7), of the breakthrough curves as predicted by the 3D numerical simulations versus the experimental ones.

where

$$\epsilon = \frac{b}{L}, \quad x = \frac{\tilde{x}}{L}, \quad y = \frac{\tilde{y}}{b}, \tag{10}$$

V_m is the dimensionless average velocity, $D_m = \tilde{D}_m/D_0$ is the effective molecular diffusion coefficient in the matrix, $\tilde{D}_m$, normalized by D_0 (Dejam *et al.*, 2014), and t is defined by Eq. (6). The dimensionless dispersion coefficient in the channel is given by

$$D_d = 1 + \frac{1}{175}\mathrm{Pe}^2. \tag{11}$$

The model is based on the assumption that the concentration distribution in the fracture is well homogenized in the y-direction and that, as a result, $\langle c_f \rangle$ is a function of only x and t. Dejam *et al.* (2014) showed that their model is capable of successfully modeling passive transport in fractures embedded in impermeable matrices for Pe numbers ranging from 10^{-2} to 10^4. Additional details about the model can be found in Dejam *et al.* (2014).

The diffusive model has two unknown parameters, V_m and D_m, and we determine them by least-square fitting. The fitted BTCs for the diffusive-matrix model are shown in Fig. 5 (dashed black lines) for all topologies, while the fitted values are listed in Table II (third column).

2. Dispersive-matrix model

The model proposed by Ling *et al.* (2016) explicitly accounts for a permeable matrix with porosity ϕ [-] and permeability k [L^2]. It describes the spatio-temporal evolution of the average pore-scale concentration in the channel and the matrix, $\langle c_f \rangle$ and $\langle c_m \rangle$, up to errors of order ϵ,

$$\mathrm{Pe}\left(\frac{\partial\langle c_f\rangle}{\partial t} + \langle u_f\rangle\frac{\partial\langle c_f\rangle}{\partial x}\right) = \epsilon D_f^\star \frac{\partial^2\langle c_f\rangle}{\partial x^2} + \phi\mathrm{Pe}\langle u_m\rangle\frac{\partial\langle c_m\rangle}{\partial x} - \frac{3\phi D_{my}}{\epsilon^2 h}(\langle c_f\rangle - \langle c_m\rangle), \tag{12a}$$

$$\mathrm{Pe}\left(\frac{\partial\langle c_m\rangle}{\partial t} + \langle u_m\rangle\frac{\partial\langle c_m\rangle}{\partial x}\right) = \epsilon D_m^\star \frac{\partial^2\langle c_m\rangle}{\partial x^2} - \frac{\mathrm{Pe}\langle u_f\rangle}{\phi h}\frac{\partial\langle c_f\rangle}{\partial x} + \frac{3D_f}{\epsilon^2\phi h}(\langle c_f\rangle - \langle c_m\rangle), \tag{12b}$$

where D_f is the dimensionless effective molecular diffusion coefficient in the channel and D_{my} is the dimensionless effective molecular diffusion coefficient in the matrix in the y-direction. Here, we set $D_f = D_{my} = 1$; i.e., the effective diffusion coefficients in the fracture and matrix are equal to molecular diffusion. The averaged dimensionless velocities $\langle u_f \rangle$ and $\langle u_m \rangle$ in the channel and matrix are the vertically averaged velocity profiles obtained by solving the coupled Stokes equation in the channel and the Darcy-Brinkman equation in the matrix (Ling *et al.*, 2016), where the dimensionless velocities u_f and u_m are obtained by normalizing $\tilde{u}_f$ and $\tilde{u}_m$ by the inlet velocity U,

$$u_f(y) = -\frac{\Psi}{2}(y^2 + Ay + B), \quad y \in (0, 1), \tag{13a}$$

$$u_m(y) = -\frac{\Psi}{\lambda^2}(1 + Ee^{\lambda y} + Fe^{-\lambda y}), \quad y \in (-h, 0), \tag{13b}$$

where

$$\Psi = \frac{b^2}{\mu U}\tilde{\nabla}\tilde{P} \tag{14}$$

TABLE II. Fitting parameters and modeling errors for each geometry calculated at $\tilde{x}$ = 8 mm.

		3D model equation (6)		Dispersive model equation (6)				Diffusive model equation (4)			
				λ	Ψ			D_m	V_m		
	Runs	t_0/T_{adv}	$E_{3D} \times 10^{-2}$	calculated		t_0/T_{adv}	$E_{Disp} \times 10^{-2}$	fitted		t_0/T_{adv}	$E_{Diff} \times 10^{-2}$
	C1-10	0.246	0.88	5.77	−75.72	0.526	1.23	1.00	100	1.047	2.44
	C1-50	0.710	0.96	7.21	−75.81	0.652	1.58	0.52	100	1.000	1.72
	C1-100	0.140	0.80	5.94	−75.72	0.020	0.58	0.46	100	0.260	1.15
	C3-10	0.246	0.71	4.63	−72.9	0.541	0.18	1.00	100	1.060	2.17
	C3-50	0.265	0.66	6.63	−73.0	0.219	0.28	0.52	100	0.570	1.40
	C1-100	0.270	0.59	6.63	−73.39	0.155	0.16	0.46	100	0.405	1.19
	R1-10	0.738	0.42	200	−124.0	0.292	0.28	0.46	16.7	0.577	0.71
	R1-50	0.636	0.98	316	−124.4	0.101	1.77	0.52	19.3	0.419	0.48
	R1-100	0.552	0.65	251	−124.3	0.051	1.15	0.32	26.8	0.057	0.52
	C2-10	0.465	0.71	17.5	−95.7	0.479	1.12	1.38	100	1.025	2.59
	C2-50	0.128	0.86	21.8	−95.6	0.113	0.83	0.52	72.0	0.203	0.09
	C2-100	0.070	1.53	21.8	−95.4	0.204	1.92	1.00	10	0.238	1.23
	R2-10	0.461	0.47	1260	−126.9	0.032	2.04	0.46	10	0.273	0.53
	R2-50	0.250	0.78	1580	−129.3	0.310	0.91	0.52	100	0.069	0.82
	R2-100	0.576	0.28	794	−128.1	0.044	1.15	0.52	1000	0.334	0.78

is the dimensionless pressure gradient (with μ the dynamic viscosity and $\tilde{\nabla}\tilde{P}$ the dimensional pressure drop). The integration constants A, B, E, and F in (13) are defined by

$$A = 2, \tag{15a}$$

$$B = 2\lambda^{-2}(-1 + e^{\lambda h})(-1 + e^{\lambda h} + \lambda + \lambda e^{\lambda h})(1 + e^{2\lambda h})^{-1}, \tag{15b}$$

$$E = e^{\lambda h}(-1 + \lambda e^{\lambda h})(1 + e^{2\lambda h})^{-1}, \tag{15c}$$

$$F = (\lambda + e^{\lambda h})(1 + e^{2\lambda h})^{-1}, \tag{15d}$$

where

$$\lambda =: \frac{1}{\sqrt{\mathrm{Da}}} = \frac{b}{\sqrt{k}} \tag{16}$$

is the square root of the inverse Darcy number. The dispersion coefficients $D_f^\star$ and $D_m^\star$ explicitly depend on λ (i.e., on the matrix permeability k) and are given by

$$D_i^\star = 1 + \mathrm{Pe}^2 I_i(\lambda, h, \Psi), \quad i = \{f, m\}, \tag{17}$$

where $I_i(\lambda, h, \Psi) = \langle u_i \int_0^y \int_0^y u_i'(y)\mathrm{d}y\mathrm{d}y\rangle$, and $u_i' = u_i - \langle u_i\rangle$ is the velocity fluctuation. For the fracture, direct integration gives

$$I_f = \frac{\Psi^2}{105}\left\{1 + \frac{7}{3}\frac{\left(e^{\lambda h} - 1\right)\left[e^{\lambda h} - 1 + \lambda(1 + e^{\lambda h})\right]}{\lambda^2(1 + e^{2\lambda h})}\right\}. \tag{18}$$

The upscaled equations (12) have the classical structure of standard advection-dispersion equations other than the last two terms in the RHS. The source/storage term $(\langle c_f\rangle - \langle c_m\rangle)$ couples the equations and describes the mass exchange between the matrix and the channel. The second term on the RHS provides an additional contribution due to concentration gradients along the channel and originates from the advective fluxes due to the presence of a matrix with non-zero finite permeability. An additional explanation about the model can be found in Ling *et al.* (2016). It is worth emphasizing that, different from the classical form of Taylor dispersion coefficient [see Eq. (11)], the dispersion coefficient in the dispersive-matrix model, defined by Eq. (17), explicitly depends on the matrix effective properties, including its permeability. The model is valid under the assumptions that $\epsilon \ll 1$ and $\mathrm{Pe} < \epsilon^{-1/2}$. Details of the model derivation and validation can be found in Ling *et al.* (2016).

All geometric parameters in the model (12)–(18), e.g., the dimensionless matrix height h, can be directly measured from the experimental setup. Instead, direct experimental measurements of the normalized pressure drop Ψ and the inverse dimensionless permeability λ, defined by (14) and (16), present challenges. On the one hand, the pressure drop cannot be accurately measured due to the relatively short length L of the microfluidic chip; on the other hand, permeability cannot be directly evaluated from tracer experiments. Here, we use the 3D pore-scale simulations developed in Sec. III A to determine Ψ and λ. Specifically, Ψ can be directly calculated from spatially averaging the inlet and outlet pressure (along the transverse cross section of the channel) once pressure distribution throughout the microchannel is numerically determined.

In order to determine the obstruction permeability k (or equivalently λ), we first average the horizontal component of the 3D velocity field $u(x, y, z)$, evaluated at $x = 0.53$, i.e., $\tilde{x} = 8$ mm, and $z = 0.5$ (with $z = \tilde{z}/H_z$), i.e., $\tilde{z} = 40$ μm, over an x–y volume of size w^2, i.e.,

$$u_{3D}(y) = \frac{1}{w^2}\int_{y-w}^{y+w}\int_{0.53-w}^{0.53+w} u(\xi, \eta, \frac{1}{2})\mathrm{d}\xi\mathrm{d}\eta,$$
$$\xi \in [0.53 - w, 0.53 + w],\ \eta \in [y - w, y + w], \tag{19}$$

to obtain an average velocity u_{3D}, which is only a function of y. We then fit the Stokes and Darcy-Brinkman velocity solutions (13) with $u_{3D}(y)$ by using λ as the fitting parameter. The spatially averaged 3D velocity profiles at the $z = 0.5$ z-plane (i.e., at the center plane of the channel, $\tilde{z} = 40$ μm) and cross section $x = 0.53$ (i.e., at the center of the channel, $\tilde{x} = 8$ mm) are plotted in Fig. 8 in gray, together with the fitted analytical solution (in black). The Ψ and λ values are listed in Table II (second column).

Once Ψ and λ are determined, the breakthrough curves can be predicted without any further calibration by solving the 1D system of Eqs. (12). The BTC predictions from the dispersive model are indicated in blue in Fig. 5. We would like to emphasize that since Ψ and λ are determined from an independent set of data (namely, 3D flow simulations), the calculated BTCs can be thought of as fit-free. This approach can be extended to fracture-matrix systems that involve natural rocks (or their 2D prints from XCT scans) where the pressure drop and permeability can be determined via core experiments. Such experiments could in fact shed new light on both the impact of realistic complex morphologies on mass and momentum transport across the fracture-matrix interface, as well as on the coupling between matrix

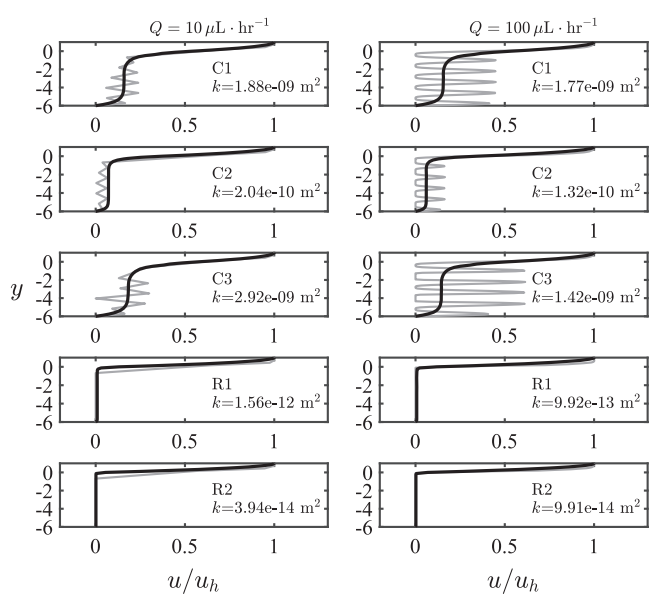

FIG. 8. Comparison between the longitudinal velocity (x-direction) calculated from Eq. (13) and the simulated velocity which is averaged from the result of Eq. (4). Gray curves are the averaged velocity profiles obtained from the 3D model, and black curves represent the fitted profiles using Eqs. (13a) and (13b).

morphology and rocks' chemical heterogeneity in the context of reactive transport.

IV. DATA COMPARISON AND DISCUSSION

The comparison between the experimental data and the three models discussed earlier is shown in Fig. 5. The experimental data are represented by open symbols, while the red, blue, and black curves are the BTCs predicted by 3D simulations, the dispersive-matrix models, and the diffusive-matrix models, respectively. The full dataset is available at https://www.digitalrocksportal.org/projects/140. To quantitatively assess the match between each model and the experimental results, we calculate the least square error

$$E_j = \frac{\sqrt{\sum_{i=1}^{N}\left(\langle c_f\rangle_{i,j} - \langle c_f\rangle_{i,\mathrm{Data}}\right)^2}}{N}, \quad j = \{\mathrm{3D, Diff, Disp}\}, \tag{20}$$

where $\langle c_f\rangle_{i,j}$ is the j-model fitted concentration at time t_i, $i = \{1, \ldots, N\}$, and the subscripts "3D," "Diff," and "Disp" refer to the 3D numerical simulations and the upscaled model that accounts for a purely diffusive matrix and dispersive matrix, described by Eqs. (4), (9), and (12), respectively. A summary of the data (least square error, fitting values, and/or predictions) pertaining the three models is presented in Table II.

Both Fig. 5 and Table II show that the fit-free pore-scale 3D simulations are in good agreement with the experimental data for all ranges of Péclet numbers and topologies, with least-square errors almost consistently less than 10^{-2}, with the exception of case C2-100.

To determine the applicability regime for the two macroscopic models, in Fig. 9, we plot the ratio $E_{\mathrm{Disp}}/E_{\mathrm{Diff}}$ for all considered geometries as a function of the Péclet number and λ. In this figure, the errors are computed at points indicated by circles, and the color map is obtained by cubic interpolation of the computed points. Figure 9 shows that

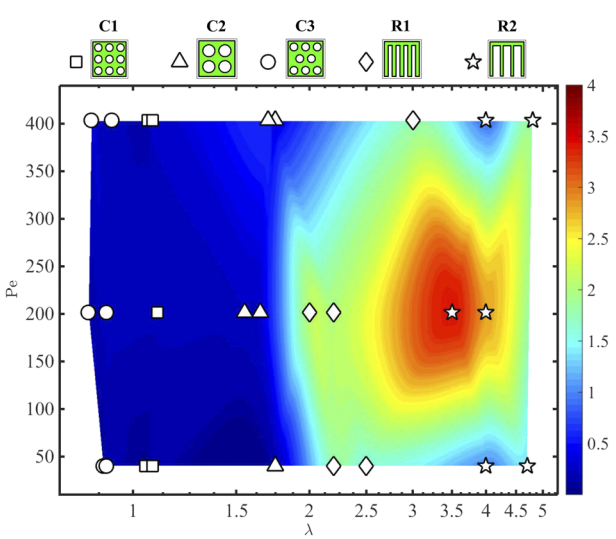

FIG. 9. Error ratio $E_{\mathrm{Disp}}/E_{\mathrm{Diff}}$ plotted in Péclet number (Pe) and λ space (Pe, λ). Symbols represent the calculated values of $E_{\mathrm{Disp}}/E_{\mathrm{Diff}}$ for any given geometry and Pe, while the color field is obtained by cubic interpolation of the measurement points.

the dispersive-matrix model (12) is more accurate than its diffusive counterpart for those structures with significant advective transport between obstacles (i.e., C1, C2, and C3) (blue region in Fig. 9, $E_{\mathrm{Disp}}/E_{\mathrm{Diff}} < 1$). Instead, the diffusive-matrix model performs better on R1 and R2 structures, where the transverse riblets block any longitudinal advective flux through the pattern and the transport inside the microstructure is mostly diffusive (red region in Fig. 9, $E_{\mathrm{Disp}}/E_{\mathrm{Diff}} > 1$). We emphasize that, while Fig. 9 provides information about the comparative performance between the dispersive and diffusive models, Table II lists the individual model errors. When Pe is large, the transport is advection driven and the concentration reaches its maximum in a very short period of time; as a result, the impact of the matrix geometry on macroscale transport is small and the error between the dispersive and diffusive models becomes similar. Instead, when Pe decreases, the influence of the geometry becomes profound: this is reflected by the domains of applicability of the different solutions. Furthermore, when $\lambda \lesssim \mathcal{O}(10)$ (i.e., high permeability values, $k \geq 10^{-10}$ m^2), the fitted values for λ have small variations for the same microstructure (C1, C2, and C3) at different Péclet numbers. This suggests that a unique permeability value k (or its dimensionless counterpart λ) can be experimentally determined for each microstructure, further validating the hypothesis that the obstruction can be treated as a continuum. On the other hand, the scatter in the fitted λ increases for R1 and R2 structures, where the effective property is ill-defined (i.e., the patterns are impermeable). We would like to emphasize that unlike the diffusive-matrix model (which contains two fitting parameters), the dispersive-matrix model is able to fully predict the BTCs for the permeable geometries once the parameters Ψ and λ are computed from the velocity field (in this particular case, the 3D simulations): for a system where the pressure and permeability are measured, or the velocity profile is known, the upscaled dispersive model can be considered fully predictive. Table II shows that structures with smaller porosity exhibit smaller permeability (e.g., C1 and C2), and permeability decreases with increasing tortuosity [the ratio between the average length of the fluid paths and the geometric length of the sample (Matyka *et al.*, 2008), Eq. (3)] for a given porosity (e.g., C1 and C3), which is consistent with well-established permeability-porosity-tortuosity relationships such as the Carman-Kozeny equation.

These results support the hypothesis that properly designed micropatterns can represent continuum-scale porous media in coupled channel/matrix systems and that microtextured channels can be employed to validate continuum-scale models of transport in coupled channel-matrix systems. Furthermore, we have experimentally validated the upscaled models proposed by Dejam *et al.* (2014) and Ling *et al.* (2016) to describe flow and transport in channels bounded by either impermeable or permeable matrices.

V. CONCLUSIONS

In this work, we have performed microfluidic experiments in channels embedded in micropatterns with different topologies. Specifically, we focus on transverse riblets and arrays of

pillars as examples of impermeable and permeable obstructions, respectively. We compare the experimental results with three models: (1) 3D pore-scale simulations which resolve the micropattern geometry explicitly and two upscaled models which treat the micropattern as a continuum. The latter are two existing models of passive transport in channel-matrix systems by (2) Dejam *et al.* (2014) and (3) Ling *et al.* (2016), where either diffusive (zero-permeability matrix or $\lambda \to \infty$) or dispersive (permeable matrix or $\lambda \to 0$) fluxes are considered, respectively.

This study suggests that (i) patterned microfluidic channels may be used as benchmark experiments to model coupled channel-matrix systems where both diffusive and advective transport effects are considered; (ii) the macroscale diffusive-matrix model by Dejam *et al.* (2014) can be successfully fitted to data when the obstruction is impermeable, e.g., the riblet structures; (iii) the macroscale dispersive-matrix model by Ling *et al.* (2016) can be successfully used for fit-free predictions of non-reactive solute transport in channel systems embedded in permeable obstructions with periodic microstructures for a wide range of Péclet numbers once relevant flow parameters are determined or measured (i.e., pressure drop and obstruction permeability); (iv) for the cylindrical obstructions, the fitted permeability values are physical, i.e., independent of operating flow conditions (Peclét number) and representative of different topologies (e.g., permeability is lower for more tortuous topologies and higher for more porous textures); and (v) the conceptualization of discrete patterns as a porous medium is appropriate since the modeling error is the same order of magnitude of the upscaling error. However, the impact of random (and/or non-periodic) matrix microstructures needs further experimental investigation.

Finally, while the conclusions obtained from this analysis cannot be directly applied to multiphase systems where the dynamics of the flowing phases is primarily controlled by instability (Ling *et al.*, 2017), a similar approach, which combines microfluidic experiments in controlled geometries, direct numerical simulations, and effective medium models, can be straightforwardly extended to multiphase systems and used to validate a number of continuum scale approximations. This is the object of current studies.

ACKNOWLEDGMENTS

I. Battiato gratefully acknowledges support by the U.S. Department of Energy Early Career Award in Basic Energy Sciences No. DE-SC0014227 "Multiscale dynamics of reactive transport in the subsurface" and the in-kind support for the experiments conducted at the EMSL user facility. B. Ling was supported through the National Science Foundation (NSF) through Award No. 1533874, "DMREF: an integrated multiscale modelling and experimental approach to design fouling resistant membranes," while performing the experiments at the Environmental Molecular Science Laboratory (EMSL). A. Tartakovsky was partially supported by the U.S. Department of Energy (DOE) Office of Advanced Scientific Computing (ASCR) as part of the Early Career Award "New Dimension Reduction Methods and Scalable Algorithms for Multiscale Nonlinear Phenomena" and DOE's Office of Biological and Environmental Research (BER) through the Pacific Northwest National Laboratory (PNNL) Subsurface Biogeochemical Research Scientific Focus Area project. PNNL is operated by Battelle for the DOE under Contract No. DE-AC05-76RL01830.

Battiato, I., "Self-similarity in coupled Brinkman/Navier-Stokes flows," J. Fluid Mech. **699**, 94–114 (2012).
Battiato, I., "Effective medium theory for drag-reducing micro-patterned surfaces in turbulent flows," Eur. Phys. J. E **37**, 19 (2014).
Battiato, I. and Tartakovsky, D. M., "Applicability regimes for macroscopic models of reactive transport in porous media," J. Contam. Hydrol. **120**, 18–26 (2011).
Battiato, I. and Rubol, S., "Single-parameter model of vegetated aquatic flows," Water Resour. Res. **50**, 6358, https://doi.org/10.1002/2013WR015065 (2014).
Battiato, I., Bandaru, P., and Tartakovsky, D. M., "Elastic response of carbon nanotube forests to aerodynamic stresses," Phys. Rev. Lett. **105**, 144504 (2010).
Bouquet, L. and Lauga, E., "A smooth future?," Nat. Mater. **10**, 334 (2011).
Cui, J., Daniel, D., Grinthal, A., Lin, K., and Aizenberg, J., "Dynamic polymer systems with self-regulated secretion for the control of surface properties and material healing," Nat. Mater. **14**, 790–795 (2015).
Deck, C., Ni, C., Vecchio, K., and Bandaru, P., "The response of carbon nanotube ensembles to fluid flow: Applications to mechanical property measurement and diagnostics," J. Appl. Phys. **106**, 074304 (2009).
Dejam, M., Hassanzadeh, H., and Chen, Z., "Shear dispersion in a fracture with porous walls," Adv. Water Resour. **74**, 14–25 (2014).
Gilroy, S. and Jones, D. L., "Through form to function: Root hair development and nutrient uptake," Trends Plant Sci. **5**, 56–60 (2000).
Goharzadeh, A., Khalili, A., and Jørgensen, B. B., "Transition layer thickness at a fluid-porous interface," Phys. Fluids **17**, 057102 (2005).
Griffiths, I. M., Howell, P. D., and Shipley, R. J., "Control and optimization of solute transport in a thin porous tube," Phys. Fluids **25**, 033101 (2013).
Gruenberger, A., Probst, C., Heyer, A., Wiechert, W., Frunzke, J., and Kohlheyer, D., "Microfluidic picoliter bioreactor for microbial single-cell analysis: Fabrication, system setup, and operation," J. Visualized Exp. **82**, e50560 (2013).
Hornung, U., *Homogenization and Porous Media* (Springer, New York, 1997).
Hou, X., Hu, Y., Grinthal, A., Khan, M., and Aizenberg, J., "Liquid-based gating mechanism with tunable multiphase selectivity and antifouling behaviour," Nature **519**, 70–73 (2015).
Korneev, S. and Battiato, I., "Sequential homogenization of reactive transport in porlydisperse porous media," Multiscale Model. Simul. **14**, 1301–1318 (2016).
Ling, B., Tartakovsky, A. M., and Battiato, I., "Dispersion controlled by permeable surfaces: Surface properties and scaling," J. Fluid Mech. **801**, 13–42 (2016).
Ling, B., Bao, J., Oostrom, M., Battiato, I., and Tartakovsky, A. M., "Modeling variability in porescale multiphase flow experiments," Adv. Water. Resour. **105**, 29–38 (2017).
Liu, C., Shang, J., Kerisit, S., Zachara, J. M., and Zhu, W., "Scale-dependent rates of uranyl surface complexation reaction in sediments," Geochim. Cosmochim. Acta **105**, 326–341 (2013).
Marschner, H. and Dell, B., "Nutrient uptake in mycorrhizal symbiosis," Plant Soil **159**, 89–102 (1994).
Maruf, S. H., Wang, L., Greenberg, A. R., Pellegrino, J., and Ding, Y., "Use of nanoimprinted surface patterns to mitigate colloidal deposition on ultrafiltration membranes," J. Membr. Sci. **428**, 598–607 (2013).
Matyka, M., Khalili, A., and Koza, Z., "Tortuosity-porosity relation in porous media flow," Phys. Rev. E **78**, 026306 (2008).
Nikora, V., Goring, D., McEwan, I., and Griffiths, G., "Spatially averaged open channel flow over rough bed," J. Hydraul. Eng. **127**, 123 (2001).
Nitsche, L. C. and Brenner, H., "Eulerian kinematics of flow through spatially periodic models of porous media," Arch. Ration. Mech. Anal. **107**, 225–292 (1989).
Papke, A. and Battiato, I., "A reduced complexity model for dynamic similarity in obstructed shear flows," Geophys. Res. Lett. **40**, 3888, https://doi.org/10.1002/grl.50759 (2013).
Petrášek, Z. and Schwille, P., "Precise measurement of diffusion coefficients using scanning fluorescence correlation spectroscopy," Biophys. J. **94**, 1437–1448 (2008).

Roubinet, D., Dreuzy, J.-R., and Tartakovsky, D. M., "Semi-analytical solutions for solute transport and exchange in fractured porous media," Water Resour. Res. **48**, W01542, https://doi.org/10.1029/2011wr011168 (2012).

Rubol, S., Battiato, I., and de Barros, F. P., "Vertical dispersion in vegetated shear flows," Water Resour. Res. **52**, 8066–8080, https://doi.org/10.1002/2016wr018907 (2016).

Rubol, S., Ling, B., and Battiato, I., "Universal scaling-law for flow resistance over canopies with complex morphology," Sci. Rep. **8**, 4430 (2018).

Stroock, A. D. and Whitesides, G. M., "Controlling flows in microchannels with patterned surface charge and topography," Acc. Chem. Res. **36**, 597–604 (2003).

Stroock, A. D., Dertinger, S. K. W., Ajdari, A., Mezic, I., Stone, H. A., and Whitesides, G. M., "Chaotic mixer for microchannels," Science **295**, 647–651 (2002).

Tang, D. H., Frind, E. O., and Sudicky, E. A., "Contaminant transport in fractured porous media: Analytical solution for a single fracture," Water Resour. Res. **17**, 555–564, https://doi.org/10.1029/wr017i003p00555 (1981).

Ul Islam, T. and Gandhi, P. S., "Fabrication of multiscale fractal-like structures by controlling fluid interface instability," Sci. Rep. **6**, 37187 (2016).

Valdes-Parada, F. J., Alvarez-Ramirez, J., Goyeau, B., and Ochoa-Tapia, J. A., "Jump condition for diffusive and convective mass transfer between a porous medium and a fluid involving adsorption and chemical reaction," Transp. Porous Media **78**, 459–476 (2009).

Weinbaum, S., Zhang, X., Han, Y., Vink, H., and Cowin, S. C., "Mechanotransduction and flow across the endothelial glycocalyx," Proc. Natl. Acad. Sci. U. S. A. **100**, 7988–7995 (2003).

Whitaker, S., *The Method of Volume Averaging* (Kluwer Academic Publishers, The Netherlands, 1999), pp. 1–70.

Willingham, T., Zhang, C., Werth, C. J., Valocchi, A. J., Oostrom, M., and Wietsma, T. W., "Using dispersivity values to quantify the effects of pore-scale flow focusing on enhanced reaction along a transverse mixing zone," Adv. Water Resour. **33**, 525–535 (2010).

Wood, B., "The role of scaling in upscaling," Adv. Water Resour. **32**, 723–736 (2009).

Zhang, C., Dehoff, K., Hess, N., Oostrom, M., Wietsma, T. W., Valocchi, A. J., Fouke, B. W., and Werth, C. J., "Pore-scale study of transverse mixing induced $CaCO_3$ precipitation and permeability reduction in a model subsurface sedimentary system," Environ. Sci. Technol. **44**, 7833–7838 (2010).